Quantitative In-Line Phase-Contrast Imaging with Multienergy X Rays

T. E. Gureyev, S. Mayo, S. W. Wilkins, D. Paganin, and A. W. Stevenson
Commonwealth Scientific and Industrial Research Organisation, PB 33, Clayton South, VIC 3169, Australia
(Received 13 October 2000)

We present a new method for quantitative nondestructive characterization of objects by x-ray phase-contrast imaging. Spatial distributions of the projected values of the complex refractive index in the sample are reconstructed by processing near-field images collected at a fixed sample-to-detector distance using a polychromatic incident beam and an energy-sensitive area detector, such as a CCD used in the photon-counting spectroscopy mode. The method has the potential advantages of decreased radiation dose and increased accuracy compared to conventional techniques of x-ray imaging.

DOI: 10.1103/PhysRevLett.86.5827 PACS numbers: 87.59.Hp, 41.50.+h, 42.30.Rx, 42.30.Va

In x-ray imaging, as in any other imaging technique where wave effects are not negligible, two basic mechanisms of contrast formation can be distinguished, namely, differential absorption and phase shifts. Several modes of x-ray phase-contrast imaging have been implemented over the years, including the holographic [1] and Zernike [2] soft x-ray microscopes, x-ray interferometry [3], single-crystal-analyzer techniques [4,5], and more recently the in-line method [6–8]. The last method, which is close in principle to Gabor's in-line holography [9], serves as a base for the development in the present paper.

According to the properties of Fresnel diffraction, free-space propagation of a beam transforms phase variations in the object plane into detectable intensity variations in the image plane, provided the latter is located at a sufficient distance from the former. Therefore, the in-line method does not require any optical elements to obtain phase contrast. It has been demonstrated that the only mandatory prerequisite for this method is a high degree of transverse spatial coherence of the incident beam, which can be achieved either with a quasiplane wave from a synchrotron source [6] or with a quasispherical wave from a microfocus laboratory source [7]. The requirements on the chromatic coherence of the beam are much less stringent [10].

It has been shown that the near-field contrast from a nonabsorbing object is proportional to the Laplacian of the phase distribution in the object plane [11–14,7]. Therefore, the projections of the real part of the refractive index of a pure phase sample can be recovered by inverse-Laplace filtering of a single near-field image [14]. However, most objects encountered in the practice of x-ray in-line imaging combine some degree of absorption contrast with phase contrast. In such cases, more than one image may be necessary for the unambiguous determination of the complex index of refraction. In the present paper, we demonstrate a new method for the determination of the complex refractive index in a sample using multiple in-line x-ray images at different energies. We first develop the theoretical framework of the new technique, then test it on numerically simulated data, and, finally, apply it to images collected at several energies using a purpose-built laboratory x-ray ultramicroscope with energy-sensitive detector and having submicron spatial resolution.

Let us first consider a plane incident wave with wavelength λ and unit intensity propagating along the optic axis z. The distributions of intensity I and phase φ in the plane orthogonal to the optic axis and located immediately after a thin weakly refracting object can be expressed in terms of line integrals of the complex index of refraction, $n \equiv n(\mathbf{r}) = 1 - \delta - i\beta$, $|n - 1| \ll 1$, $\mathbf{r} = (\mathbf{r}_\perp, z)$, $I(\mathbf{r}_\perp, 0, \lambda) = \exp[-M(\mathbf{r}_\perp, 0, \lambda)]$,

$$M(\mathbf{r}_\perp, 0, \lambda) = (4\pi/\lambda) \int_{-\infty}^{0} \beta(\mathbf{r}_\perp, z', \lambda)\, dz', \qquad (1)$$

$$\varphi(\mathbf{r}_\perp, 0, \lambda) = -(2\pi/\lambda) \int_{-\infty}^{0} \delta(\mathbf{r}_\perp, z', \lambda)\, dz'. \qquad (2)$$

The dependencies of the real and imaginary parts of the absorption coefficient on the wavelength of the incident radiation in the absence of absorption edges between λ_0 and λ, for any elements present in the sample, are well known [15]:

$$\beta(\lambda) = (\lambda/\lambda_0)^4 \beta(\lambda_0), \qquad \delta(\lambda) = (\lambda/\lambda_0)^2 \delta(\lambda_0). \qquad (3)$$

The propagation of the beam from the object plane $z = 0$ to the image plane $z = R$ can be described mathematically by the Fresnel integral. In the near field, i.e., in the region where the Fresnel number is large, the square modulus of the Fresnel integral can be approximated using the transport of intensity equation (TIE) [11,12,16]:

$$(R\lambda/2\pi)[-\nabla^2 \varphi(\mathbf{r}_\perp, 0, \lambda) - \nabla\varphi(\mathbf{r}_\perp, 0, \lambda) \cdot \nabla \ln I(\mathbf{r}_\perp, 0, \lambda)] = I(\mathbf{r}_\perp, R, \lambda)/I(\mathbf{r}_\perp, 0, \lambda) - 1. \qquad (4)$$

Note that in the region of validity of Eq. (4) (in the near field), intensity distributions in the object and image planes cannot differ much, i.e., $|I(\mathbf{r}_\perp, R, \lambda)/I(\mathbf{r}_\perp, 0, \lambda) - 1| \ll 1$. Therefore the right-hand side (rhs) of Eq. (4) can be written as $\ln[I(\mathbf{r}_\perp, R, \lambda)] - \ln[I(\mathbf{r}_\perp, 0, \lambda)]$. Taking Eqs. (1)–(3) into account, we can now rewrite Eq. (4) as

$$-\sigma^3 M(\mathbf{r}_\perp, 0, \lambda_0) + \gamma\sigma(-\nabla^2\varphi)(\mathbf{r}_\perp, 0, \lambda_0) + \gamma\sigma^4 \nabla\varphi(\mathbf{r}_\perp, 0, \lambda_0) \cdot \nabla M(\mathbf{r}_\perp, 0, \lambda_0) = \ln[I(\mathbf{r}_\perp, R, \lambda)], \quad (5)$$

where $\sigma = \lambda/\lambda_0$ and $\gamma = R\lambda/(2\pi)$. If images at three different wavelengths λ_i, $i = 0, 1$, and 2, are available, we can consider the following system of three linear equations:

$$A\begin{pmatrix} M(\mathbf{r}_\perp, 0, \lambda_0) \\ -\nabla^2\varphi(\mathbf{r}_\perp, 0, \lambda_0) \\ \nabla M \cdot \nabla\varphi(\mathbf{r}_\perp, 0, \lambda_0) \end{pmatrix} = \begin{pmatrix} F_0 \\ F_1 \\ F_2 \end{pmatrix}, \quad \text{where } A = \begin{pmatrix} -1 & \gamma_0 & \gamma_0 \\ -\sigma_1^3 & \sigma_1\gamma_1 & \sigma_1^4\gamma_1 \\ -\sigma_2^3 & \sigma_2\gamma_2 & \sigma_2^4\gamma_2 \end{pmatrix}, \quad (6)$$

and the rhs functions $F_i = \ln[I(\mathbf{r}_\perp, R, \lambda_i)]$ can be evaluated from the three measured intensity distributions in the image plane $z = R$ at the three selected wavelengths. It can be easily verified that the determinant of the matrix A cannot be equal to zero as long as all three wavelengths λ_i, $i = 0, 1$, and 2, are different. Therefore, the projected attenuation M and the Laplacian of the phase distribution can be obtained as solutions to the linear system (6). The phase distribution can be retrieved by solving the Poisson equation, $-\nabla^2\varphi(\mathbf{r}_\perp, 0, \lambda_0) = \sum A_{1j}^{-1} F_j$, where A_{1j}^{-1}, $j = 0, 1$, and 2, are the elements of the central row of the matrix inverse to A. Any uniform boundary conditions can be used if the sample is fully contained in the field of view, although the flat-field (no sample) image may be required to correct for effects of nonuniform illumination. A number of different numerical techniques based, e.g., on the fast Fourier transform or Mutigrid methods can be used for numerical solution of the Poisson equation for the phase [16]. The projected values of the complex refractive index $n = 1 - \delta - i\beta$ can then be trivially found using Eqs. (1) and (2).

If the third term in the lhs of Eq. (5) is much smaller than the first two and can be neglected, then the system Eq. (6) can be reduced to only two equations with respect to the unknowns $M(\mathbf{r}_\perp, 0, \lambda_0)$ and $-\nabla^2\varphi(\mathbf{r}_\perp, 0, \lambda_0)$. The solution to this reduced 2×2 linear system is given by

$$M(\mathbf{r}_\perp, 0, \lambda_0) = (\lambda_0/\Delta\lambda)(F_0 - \sigma^{-2}F_1), \quad (7)$$

$$-\nabla^2\varphi(\mathbf{r}_\perp, 0, \lambda_0) = 2\pi/(R\Delta\lambda)(\sigma F_0 - \sigma^{-2}F_1), \quad (8)$$

where $\Delta\lambda = \lambda_1 - \lambda_0$ and $\sigma \equiv \sigma_1 = \lambda_1/\lambda_0$. Therefore, in this case intensity and phase in the object plane (and, hence, the projections of the complex refractive index) can be found from only two images $F_i = \ln[I(\mathbf{r}_\perp, R, \lambda_i)]$, $i = 0, 1$, collected at two different wavelengths λ_0 and λ_1.

Generalizations of the above results to the case of a spherical and/or partially coherent incident wave are straightforward [16–19].

To test the above theory, we performed the following numerical experiment. First, we chose three x-ray wavelengths, $\lambda_0 = 1$ Å, $\lambda_1 = 1.2$ Å, and $\lambda_2 = 0.8$ Å. We then simulated distributions of intensity and phase in the object plane at $\lambda = \lambda_0$ as shown in Figs. 1(a) and 1(b). The 2D numerical grid had 128×128 pixels and was assigned a physical size of (200×200) μm. Maximum absorption at λ_0 was 5%, and maximum absolute phase shift was 0.91 rad. We applied the scaling equations (3) to obtain the data at the other two wavelengths.

We then calculated the intensity distributions in the image plane $R = 2$ cm at each of the wavelengths by computing Kirchhoff integrals. The image at $\lambda = \lambda_0$ is presented in Fig. 1(c), showing both amplitude and phase contrast. The images at $\lambda = \lambda_{1,2}$ visually looked very similar. Applying the above theory [Eq. (6)] to the computed images, and solving the Poisson equation for the phase, we retrieved the intensity and phase distributions in the object plane. The results are shown in Figs. 1(d) and 1(e). The relative rms errors in the reconstructed intensity and phase both were less than 1%. As is evident in Fig. 1(f), these errors were concentrated primarily in high spatial frequency components, for which the TIE approximation to the Kirchhoff integrals is not sufficiently accurate [16].

The essentials of our experimental setup for this work are in Fig. 2, with further details available in [20].

The x-ray phase ultramicroscope used to collect the present images is based on a modified Hitachi S-450LB scanning electron microscope. A point source of x rays was generated by focusing the 25 keV electron beam into a $\sim$0.25 μm spot on a tilted target consisting of a 0.25 μm thick tantalum foil. This generated an x-ray spectrum which includes the characteristic Ta $M\alpha$ lines ($\sim$1.7 keV) along with a broad bremsstrahlung spectrum at higher energies. The sample and charge-coupled device (CCD) detector were mounted in the horizontal plane level with the

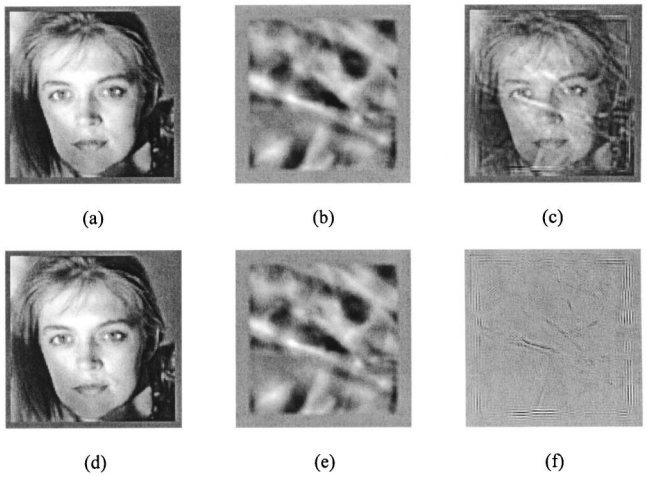

FIG. 1. Simulated distributions of (a) intensity and (b) phase in the object plane; (c) image at $\lambda_0 = 1$ Å and $R = 2$ cm; reconstructed distributions of (d) intensity and (e) phase; (f) difference between the original and reconstructed intensity distributions.

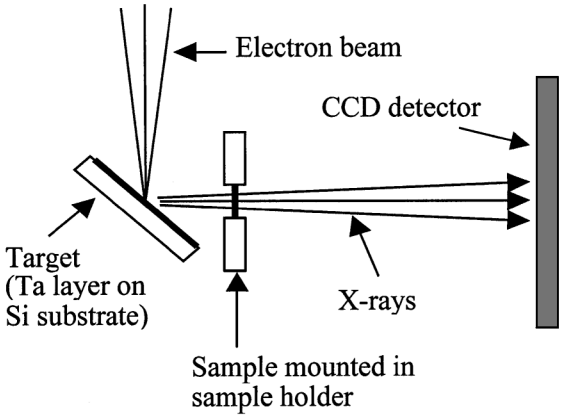

FIG. 2. Schematic diagram of experimental setup.

target and at right angles to the vertical electron beam. All images were collected using a 512 × 512 Loral CCD array with 15 μm pixels. This was used in direct detection mode (i.e., without a phosphor screen) and was Peltier cooled to 232 K in order to minimize dark current generation during long exposures.

In order to produce energy-resolved images, data were collected as a series of short exposures. In each exposure, single photon events can be identified where a bright pixel is surrounded by dark pixels. The photon energy of such events is determined by the size of the signal in the bright pixel. Energy-resolved images can be produced by selecting only events with a certain energy range when adding the data from the different exposures to form an image. In this way, a series of images with different energy ranges can be extracted, and since the data at all energies is collected simultaneously all the images will be perfectly aligned with one another. This avoids registry problems that can occur when collecting a series of images at different positions along the optic axis [16].

Images of a set of approximately 9 μm diameter latex spheres at three different energies (wavelengths) [$E_0 = 3.3$ keV ($\lambda_0 = 3.8$ Å), $E_1 = 1.7$ keV ($\lambda_1 = 7.3$ Å), and $E_2 = 5.0$ keV ($\lambda_2 = 2.5$ Å)] were collected in the above fashion. These images are presented in Fig. 3. The source-to-sample distance was $R_1 = 1.2$ mm and the sample-to-detector distance was $R_2 = 181.8$ mm. Therefore, the magnification was equal to 153, the effective propagation distance was $R = R_1R_2/(R_1 + R_2) = 1.19$ mm, and the effective pixel size at the object plane was 0.098 μm. The spatial resolution achieved in the experiment was primarily limited by the source size of ~0.25 μm. The maximum theoretical phase shift in 9 μm of latex at $E_0 = 3.3$ keV was $-\varphi_{\max}^{\text{theor}} = 3.31$ rad, and the maximum attenuation was $M_{\max}^{\text{theor}} = 0.056$. A dark vertical line visible in the right side of each image in Fig. 3 is a defect of the CCD.

We first used Eq. (6) to retrieve the amplitude and the phase in the object plane from 450 × 450 pixel subimages of Figs. 3(a)–3(c). The corresponding reconstructed phase distribution is shown in Fig. 4(a).

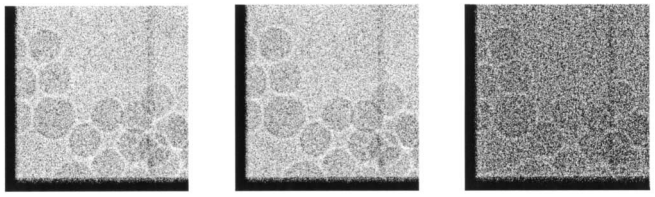

FIG. 3. Experimental images at (a) $E = 3.3$ keV, (b) 1.7 keV, and (c) 5.0 keV.

Obviously, the result contains a large amount of low-frequency noise, which is typical for the solutions of a Poisson equation with a noisy rhs function [14]. Closer analysis showed that the noisiness of the result is mainly due to the very low signal-to-noise ratio in the image collected at the highest energy, where attenuation and phase shifts were the smallest [see Fig. 3(c)]. Therefore, we decided to exclude that image from the set of experimental data and use the approximation assumed in Eqs. (7) and (8). This approximation was applicable to our experimental data as the theoretically estimated attenuation was small, $M_{\max}^{\text{theor}} = 0.056$, and it was not changing very rapidly. The distributions of the phase φ and attenuation M in the object plane reconstructed from images 3(a) and 3(b) using Eqs. (7) and (8) are presented in Figs. 4(b) and 4(c).

The maximum phase shift averaged over a 20 × 20 pixel area in the middle of single spheres marked by numbers 1–4 in Fig. 4(b) are presented in the first row of Table I. The corresponding value obtained from an ideal latex sphere of 9 μm diameter at $E_0 = 3.3$ keV was $\langle -\varphi_{\max}^{\text{theor}} \rangle = 3.25$ rad; therefore, the reconstructed values are in a very good agreement with the theoretical prediction. The sphere No. 5 in Fig. 4(b), which looked noticeably larger than the others, had a value of $\langle -\varphi_{\max}^{\text{exp}} \rangle = 4.50$, which corresponded to the diameter of 12.5 μm. The estimation of the diameter of this sphere obtained from Fig. 3(b) was equal to 118 pixels or 11.6 μm. The region No. 6 gave $\langle -\varphi_{\max}^{\text{exp}} \rangle = 7.27$ rad, and the region No. 7 gave $\langle -\varphi_{\max}^{\text{exp}} \rangle = 5.64$, which would appear to indicate that there are spheres stacked on top of each other in these locations. The maximum values of attenuation averaged over a 20 × 20 pixel area in the

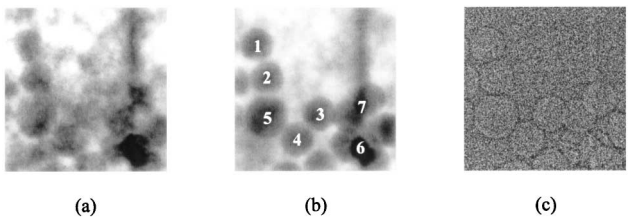

FIG. 4. Reconstructions from 450 × 450 pixel subimages: (a) phase from Figs. 3(a)–3(c); (b) phase from Figs. 3(a) and 3(b); (c) attenuation (M) from Figs. 3(a) and 3(b).

TABLE I. Theoretical and experimental values of x-ray ($E_0 = 3.3$ keV) phase shift and attenuation in 9 μm latex spheres.

	Theory	Sphere 1	Sphere 2	Sphere 3	Sphere 4
$\langle -\varphi_{\max} \rangle$	3.25	3.20	3.53	3.57	3.12
$\langle M_{\max} \rangle$	0.055	0.061	0.070	0.053	0.056

middle of single spheres in Fig. 4(c) corresponding to spheres No. 1–4 in Fig. 4(b) are presented in the second row of Table I. These values are in good agreement with the theoretically predicted value of $\langle M_{\max}^{\text{theor}} \rangle = 0.055$.

The fact that we were able to obtain quantitatively accurate values of the projected refractive index of the sample from quite noisy experimental images indicates a good stability of the method. This can be explained by the mathematical stability of the operations involved in the reconstruction, i.e., the inversion of a very small (3×3 or 2×2) matrix combined with the inverse-Laplace filtering in the case of phase.

In conclusion, we have presented a theoretical and experimental demonstration of a new method for rapid quantitative nondestructive analysis of thick optically opaque samples. The proposed method is relatively simple experimentally. The required images at different x-ray energies can be obtained either by tuning the energy of incident x rays with a suitable source and monochromator or, preferably, by using a polychromatic incident beam and energy-sensitive x-ray area detector. We believe that this new method will be useful in material sciences, biology, and, particularly, in medical applications, where it may lead to a decrease in radiation dose to the specimens, as well as improved speed and accuracy of the experiment compared to conventional x-ray imaging techniques.

The authors acknowledge the funding and support of X-Ray Technologies Proprietary Ltd. (XRT) for this research.

[1] C. Jacobsen, M. Howells, J. Kirz, and S. Rothman, J. Opt. Soc. Am. A **7**, 1847–1861 (1990).
[2] G. Schmahl, D. Rudolph, G. Schneider, P. Guttmann, and B. Neimann, Optik **97**, 181–182 (1994).
[3] U. Bonse and M. Hart, Appl. Phys. Lett. **6**, 155–156 (1965).
[4] V. N. Ingal and E. A. Beliaevskaya, J. Phys. D, Appl. Phys. **28**, 2314–2317 (1995).
[5] T. Davis, D. Gao, T. Gureyev, A. Stevenson, and S. Wilkins, Nature (London) **373**, 595–598 (1995).
[6] A. Snigirev, I. Snigireva, V. Kohn, S. Kuznetsov, and I. Schelokov, Rev. Sci. Instrum. **66**, 5486–5492 (1995).
[7] S. W. Wilkins, T. E. Gureyev, D. Gao, A. Pogany, and A. W. Stevenson, Nature (London) **384**, 335–338 (1996).
[8] P. Cloetens, R. Barrett, J. Baruchel, J.-P. Guigay, and M. J. Schlenker, J. Phys. D, Appl. Phys. **29**, 133–146 (1996).
[9] D. Gabor, Nature (London) **161**, 777–778 (1948).
[10] A. Pogany, D. Gao, and S. W. Wilkins, Rev. Sci. Instrum. **68**, 2774–2782 (1997).
[11] J. M. Cowley, *Diffraction Physics* (North-Holland, Amsterdam, 1975).
[12] M. R. Teague, J. Opt. Soc. Am. **73**, 1434–1441 (1983).
[13] D. Van Dyck and W. Coene, Optik **77**, 125–128 (1987).
[14] K. A. Nugent, T. E. Gureyev, D. F. Cookson, D. Paganin, and Z. Barnea, Phys. Rev. Lett. **77**, 2961–2964 (1996).
[15] U. W. Arndt and B. T. M. Willis, *Single Crystal Diffractometry* (Cambridge University, Cambridge, England, 1966), p. 185.
[16] T. E. Gureyev and S. W. Wilkins, J. Opt. Soc. Am. A **15**, 579–585 (1998).
[17] T. E. Gureyev and S. W. Wilkins, Opt. Commun. **147**, 229–232 (1998); **154**, 391(E) (1998).
[18] D. Paganin and K. A. Nugent, Phys. Rev. Lett. **80**, 2586–2589 (1998).
[19] T. E. Gureyev, Optik **110**, 263–266 (1999).
[20] S. W. Wilkins, S. C. Mayo, T. E. Gureyev, P. Miller, A. Pogany, A. W. Stevenson, D. Gao, and D. Paganin (to be published).